Journal of
Materials Chemistry B

ROYAL SOCIETY
OF CHEMISTRY

PAPER

View Article Online
View Journal | View Issue

Check for updates

Cite this: *J. Mater. Chem. B*, 2024, **12**, 2746

Concentration-tuned diverse response to selective biogenic amines using a reusable fluorophore: monitoring protein-rich food spoilage†

Madhuparna Chakraborty, Pandiyan Sivasakthi, Pralok K. Samanta and Manab Chakravarty*

Received 30th October 2023,
Accepted 3rd February 2024

DOI: 10.1039/d3tb02569a

rsc.li/materials-b

Maintaining the freshness of food is essential for a healthy and quality life. Nevertheless, it remains a global challenge. Hence, an easy detection and monitoring protocol would be highly desirable. A cyanoacrylic acid (CAA)-based fluorophore is manifested as a reusable platform that responds diversely against different concentrations of selective aliphatic biogenic amines (BAs) in both solution and vapor phases. Slow spoilage of the protein-rich food is progressively monitored through emission shifts visible to the naked eye. This fluorophore provides easy and naked-eye detection of the BA vapor through a change in emission, *i.e.*, red → orange → orange-yellow → cyan → green and quantum yield enhancement, which occur in stepwise increments of vapor concentrations. The probe design includes π-conjugated functionalized fluorescent molecules linked to multiple twisting sites, resulting in both solid and solution-state emission. The attached carboxylic acid responds quickly with selective BAs, mainly putrescine (PUT), cadaverine (CAD), and spermidine (SPM), where the concentration-based emission variation has appeared to be distinct and prominent against PUT [sensitivity (μM): 2 (solution); 3.3 (vapour)]. The selectivity towards diamine can be clarified by the formation of carboxylic acid salts and the consequent proton exchanges between free and protonated amines. In addition, $-C\equiv N\cdots H$ interaction is likely to develop within this ammonium carboxylate system, providing extra stability. Such ammonium carboxylate salt formation and gradual change in the molecular arrangement, resulting in symmetry development, are validated by FT-IR and wide-angle X-ray diffraction studies. Besides, this fact is supported by DFT studies that validate intramolecular H-atom exchange between free amine and ammonium salt units. A fluorophore-coated coverslip, filter paper, or silica gel-coated Al-plate is fruitfully utilized to detect the freshness of fish and chicken, which reveals the potential of this probe to prevent food waste and control food safety.

Introduction

The entwined relationship between societal development and nutrition will collapse if food safety and food waste are poorly monitored. Hence, measuring and tracking the freshness of food from producers to consumers has become a looming challenge globally.[1–3] Among many other parameters, biogenic amines (BAs) are essential biomarkers to detect the freshness of protein-rich food.[4–7] The BAs are important metabolites for cell growth and neural transmission but also cause acute toxicity after reaching a certain level (>20 mg kg^{-1}).[8] By considering different classifications of BAs, aliphatic ones such as putrescine (PUT), cadaverine (CAD), and spermidine (SPM) offer a significant presence to flora and fauna due to an easy enzymatic and thermal decarboxylation of the corresponding amino acids.[9,10] Both CAD and PUT are foul-smelling compounds found in decaying animals and cause food poisoning, gastrointestinal damage, tachycardia, asthma, and abnormal blood pressure. Further, it affects the mammalian brain by influencing depression by augmenting the toxic effect of histamine and is responsible for bad breath and the foul smell of decaying corpses.[11,12] CAD and PUT have been found in nature, emanating from flowers in the forest area.[13] The enzymatic conversion of these BAs shows a significant demand for rapid and ultrasensitive detection to maintain food freshness. The conventional approaches to detecting BAs include expensive analytical techniques like HPLC, GC, capillary electrophoresis, and electrochemical and enzymatic methods.[14–16] However, the detection involves

---

*Department of Chemistry, Department of Chemistry, Birla Institute of Technology and Science-Pilani, Hyderabad Campus, Hyderabad-500078, India.
E-mail: manab@hyderabad.bits-pilani.ac.in1*

† Electronic supplementary information (ESI) available. CCDC 2262179. For ESI and crystallographic data in CIF or other electronic format see DOI: **https://doi.org/10.1039/d3tb02569a**

time-consuming, complex, and costly procedures and skilled professionals.[17,18] Therefore, developing a handy and portable sensor for rapid on-site BA detection is essential. In response to these challenges, various cost-effective optical-based sensors have emerged as sensitive protocols;[19–22] however, the pitfalls of these probes include (i) non-reusability and poor color-contrast, (ii) scarcity of dyes for concentration-tuned detection of BAs (an urgent need to avoid food wastage) (iii) multistep synthesis of the probe using a high energy-consumption protocol (iv) restriction to solution state emission only (v) lack of sensitivity and selectivity (vi) most importantly, lack of vapor-responsive dyes, and (vii) practical applicability for effective and quick testing of chicken or fish.[23–25] Moreover, a typical fluorophore shows its response only by fluorescence quenching mechanism *via* a chemical reaction of an amine with an electrophilic center (emission quenching is not preferred due to misguided promises).[26–28] In this context, AIE-switching was realized to detect BAs with a dye that was synthesized using harsh reaction conditions, and detection in the solid state could have been more impressive and recyclable.[29,30] Fluorophores were established to recognize PUT,[31,32] but fluorophore-based special recognition for selective PUT is sporadic. Apart from a report on the polymer-appended system,[18] small molecules, **A-B** (Fig. 1), were identified earlier for selective PUT detection with significant drawbacks.[33,34]

This work focuses on the design of new small fluorophores (mainly **TCNA**, Fig. 1) that reversibly and quickly detect PUT selectively with higher sensitivity, along with an indication for the presence of two other vital BAs [cadaverine (CAD) and spermidine (SPM)] in both solution and vapor phases. However, the response difference between CAD/SPM and PUT solutions can be readily envisioned through the naked eye. Excitingly, this probe exhibits a concentration-based rapid detection of PUT vapor [0.292 mg L^{-1} (3.3 μM)], and the solid-state emission variation is very much detectable (red to green for PUT; red to yellow for CAD/SPM) through naked-eye under a 365 nm UV lamp irradiation. Although these probes exhibit a dual-state emissive nature,[35,36] we highlight the solid-state emission switching by exposing BA vapors due to their practical desirability and handling suitability. A detailed inspection shows a change in the wide-angle X-ray diffraction (WAXRD) pattern of the emissive solid exposed to diverse PUT vapor concentrations. Experimental outcomes confirm amino-carboxylate salt formation with BAs, keeping a free –NH$_2$ group intact. The selectivity with biogenic amines corresponds to the cooperativity effect to produce an intermolecular $-C\equiv N\cdots H$ interaction (a rare event) with the appropriate cyano-functionality. A gradual enhancement in BA concentrations and modulation of supramolecular interactions will lead to the stepwise formation of salt and intermolecular H-bonding. The variation in crystallinity (as shown in WAXS) and FT-IR data validate the role of intermolecular $-C\equiv N\cdots H$ interactions. Such an approach is inimitable in this valuable research field, facilitating easy freshness detection for protein-rich food. The concentration-based variation in emission is also commendable and suitable for intelligent food packaging.[1] Further, a new inexpensive thin film-based platform is invented to detect spoiled fish and chicken by observing the gradual emission change through the naked eye. This strategy also enables the platform to be reusable more than six times. The molecular packing and available void space were also considered for effective interactions of specific BAs with admirable sensitivity.

Results and discussion

Design and synthesis of simple and suitable molecular probes

While designing a suitable molecule (Fig. 1), the following points are considered: (a) strong emission in solution: extensive π-conjugations with a prominent fluorophore, *i.e.* anthracene core (b) emissive in solid: introduction of a tiny flanking donor,[37,38] thiophene, and another substituted vinyl stator, which offers conformational twists and avoid strong

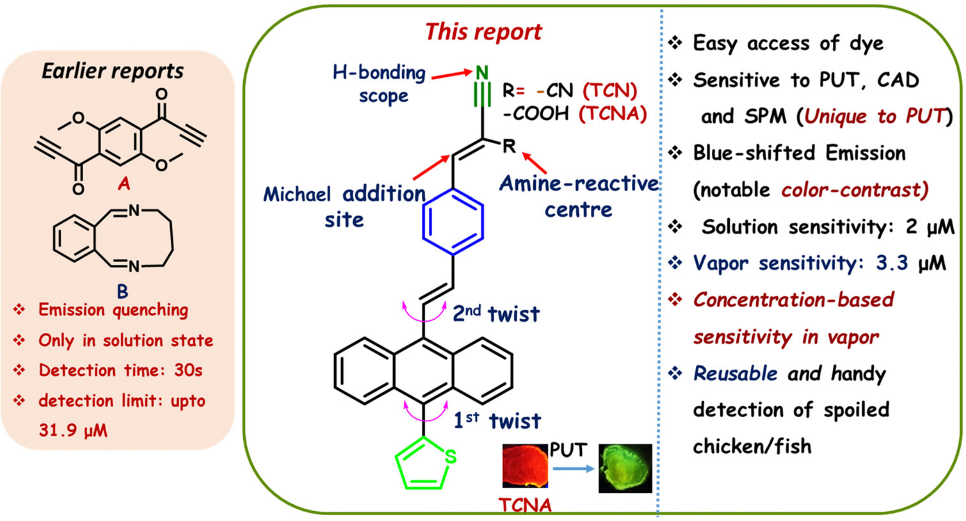

Fig. 1 Known probes **(A-B)** and our design for selective PUT-sensitive small molecule.

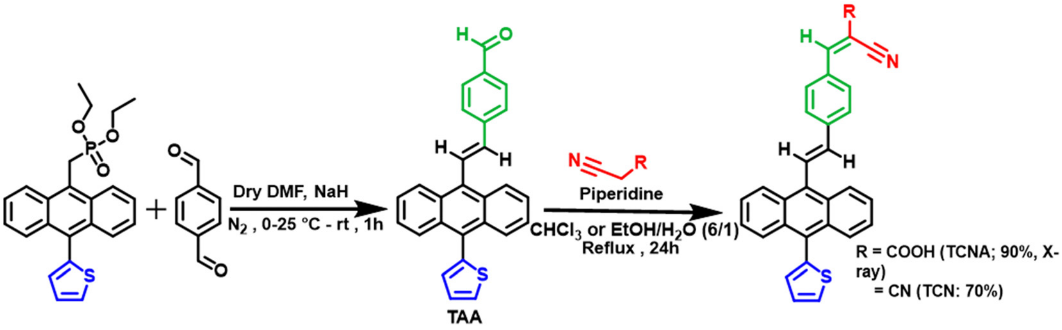

Scheme 1 Synthesis of fluorophores; for TCN: EtOH/water mixture (6 : 1) was used as a solvent.

intermolecular π···π stacking and restricted motion in the solid state, resulting in radiative decay profiles (emissive solid), (c) site for amine attack as primarily employed in the literature[39–41] through (i) Michael addition where amine acts as a substantial Michael donor, and therefore Michael acceptor site was generated in this probe by adding acrylic dicyano (**TCN**) or cyano-acid (**TCNA**) functionality, (ii) –COOH group was connected to rapidly produce the amine carboxylate salt and change the probe's emission profile (d) acrylic cyano group can facilitate inter/intramolecular interactions between cyano and $-NH_2$ groups of BAs.[42,43] Moreover, this whole strategy can adjust its reversibility by neutralizing the salt using acid vapor and making this probe recyclable.

The designed molecule was conveniently synthesized without expensive metal/ligand-catalyzed reactions, as shown in Scheme 1. Thiophene-linked anthracenyl phosphonate was introduced earlier using a simple electrophilic aromatic substitution reaction.[37,38] The same phosphonate was utilized in a partial olefination reaction with a controlled concentration of terephthaldehyde to produce **TAA** in 50% yield in pure form (unreacted phosphonate was recovered). As a suitable substrate for the Knoevenagel reaction, **TAA** was converted to our target molecules **TCN** and **TCNA**, which are ideal for Michael reactions and salt formation. All the synthesized compounds are well characterized by FT-IR, multinuclear-NMR, Mass, and single-crystal X-ray diffraction studies (only **TCNA**).

Photophysical studies

Photophysical features were examined at the outset for all three compounds: **TAA**, **TCN**, and **TCNA**. The maximum absorption at $\lambda_{max} \sim$ 397–405 nm (for **TAA** and **TCNA**) and $\lambda_{max} \sim$ 422–440 nm (for **TCN**) appeared in the absorption spectra by changing different polar solvents (Fig. S1, ESI†). The emission profiles demonstrate a nearly no/feeble emission at $\lambda_{max} \sim$ 500 nm for **TAA** in the solution state, possibly because of multiple rotors against the olefinic stator. Even solvent polarity variation did not exhibit visually detectable variation in the emission (Fig. S2a, ESI†). However, **TCNA** and **TCN** display superior emission profiles in different solvents [relative Φ_f (%) = 9 and 11, respectively, in 1,4-dioxane; (Fig. S2b and S3, ESI†)] as compared to **TAA**. Both **TCN** and **TCNA** exhibited a bathochromic shift and weaker emission in relatively more polar solvents such as MeCN. The yellow emission of **TCNA** at $\lambda_{max} \sim$ 560 nm in dioxane was chosen for subsequent studies to avoid solubility and safety issues. The optical purity of the sample is further validated with almost similar absorption and excitation spectra (Fig S3a, ESI†).

Aggregation-induced emission (AIE)-feature

Twisted rotors across the olefinic stator can restrict intramolecular motion and enhance the fluorescence (FL) in the aggregate state.[44,45] With this thought, AIE studies were performed for all these compounds. Interestingly, **TAA** and **TCN** showed an interesting AIE feature with an intensity enhancement upon gradually adding water [fraction of water f_w (v/v)] in 10 μM acetonitrile solution. The FL intensity was boosted 10–14 times with a typical redshift [Fig. S4, S5 for spectra, Fig. S7a, b for I/I_0 *vs.* f_w plot (I_0: FL intensity before adding water and I: FL intensity after the addition of water), ESI†] for both **TAA** and **TCN**, which turned into yellow and red emissive molecules in the aggregate state, respectively. However, **TCNA** was not emissive in the aggregate form; instead, it shows FL quenching under this acetonitrile/water binary solvent system (see Fig. S6 and S7c, ESI†). As **TCNA** differs only with a $-CO_2H$ functionality, its dimerization tendency in the aggregate state might favor emission quenching. Comparative detailed studies to decipher the dissimilar AIE features have recently been explored.[38a] However, the responses of amines in the solution and aggregated state are herein investigated.

Fluorescence response influenced by amines in solution/aggregated states

Indeed, all these suitably functionalized fluorophores deserve responses against amines. The aldehyde group of **TAA** can spontaneously react with amine, and the resulting emission may differ.[46a] Further, **TCN** holds an interactive site for the amine, an influential Michael donor.[46b] Therefore, we have initially explored all these probes with various amines, including BAs. Before any spectroscopic investigations, fluorophores **TAA** and **TCN** (10 μM) in 1,4-dioxane solution were screened with a wide range of amines such as aniline, triphenylamine, diphenylamine, triethylamine, 2-phenylethylamine, tryptamine, *N*-ethyldiisopropylamine, spermine, spermidine (SPM), 1,3-diamino propane (1,3-DAP), putrescine (PUT), cadaverine

(CAD) and 1,6-diaminohexane. However, no significant color change was visualized (Fig. S8a and b, ESI†) for weakly emissive **TCN** and **TAA** solutions. Further, decently emissive AIE states of **TAA** and **TCN** molecules were treated with the amine solution (1 mM in DMAc). Unfortunately, the emission from the aggregated dye for **TCN** and **TAA** remained unchanged (Fig. S9 and S10, ESI†). It indicates that these amines do not respond against aldehyde or towards Michael addition reactions under ambient conditions. A strong electron-rich environment of such fluorophores might hinder the approach of amines towards reactive centers, and extensive electronic conjugations reduce the nucleophilicity of –CHO functionality.

Next, numerous amines (1 mM in DMAc) were added to the yellow emissive **TCNA** solution in dioxane (10 μM). The optical density is somewhat reduced, but there is no appreciable change in the absorption $\lambda_{\max}$. However, a blue-shifted emission from yellow to cyan or green was visualized in the naked eye only for three vital BAs (PUT, CAD, and SPM), which are realized to be responsible for protein-rich food spoilage. Moreover, the maximum shift of 32 nm, resulting in bluish cyan, is notable upon adding PUT solution (see Fig. 2). SPM displays cyano emission with a 23 nm shift, but CAD shows a green emission with only a 15 nm shift. These results designate the specificity towards BAs in the solution state, and that too with slightly longer chain lengths because 1,3-DAP and ethylene diamine did not display any emission change (Fig. 2).

This observation has motivated us to focus on these three BAs individually. Upon treating these individual amines with **TCNA** solution, a superior sensitivity was noted with PUT compared to CAD and SPM, as presented in Fig. 3 (see Table S1 for the gradual shifts, ESI†). A clean emission shift was detectable with the lowest concentration of PUT as 1–5 μM and CAD/SPM as 4–12 μM, much lower than the required freshness detection limit (in the range of mM).[8b]

The absorption spectra of **TCNA** did not change upon gradually adding PUT, CAD, and SPM (Fig. S11, ESI†). It indicates no significant interactions between **TCNA** and these BAs in the solution state under ambient light. However, the observed emission changes upon the gradual addition of BAs were notable. It is pertinent to specify that the acidity of the dye and basicity of BAs will increase in the excited state, promoting amine-acid interactions.[47,48] The newly formed ammonium carboxylate anion will diminish electron flow from the aromatic rings to the electron-deficient cyanocarboxylate part, resulting in a blue-shifted emission. Also, lifetime studies (Fig. S12 and Table S2, ESI†) indicate a diminution in the excited state lifetime on gradual enhancement in amine concentration, demonstrating a dynamic quenching behavior.

Photophysical features in the solid state and response to BA vapors

While exposing to various amine vapors on the thin film of **TCNA** using 30 μL of amine liquid in a 200 mL closed jar under identical conditions for 15–20 min, we recognized a blue-shifted emission upon exposure to most of the amines (Fig. 4) except ammonia and spermine (see Fig. 4b: images 2, &12). Like the solution state, blue-shifted emission in a solid state is due to the lack of electronic conjugation after the ammonium carboxylate salt formation (discussed later). After exposing the amine fumes for half an hour, we recorded the emission spectrum and absolute Φ_f (%) for all these films (see Table S3, ESI†). These important BAs display the maximum blue-shifted emission and enhanced Φ_f (%), as presented in Fig. 4c. Notably, the emission shift (91 nm) with PUT vapor was the longest (Fig. 4a–c) and could be easily discriminated from the changes created by other amines (including other BAs).

With the estimated vapor pressure (mm Hg) at 25 °C, [Put 2.3, Cad 0.97, SPM 0.027], PUT can better flow in the air freely, at least with a half-life of 6 h.[13] Therefore, we emphasized the detection of BA vapors using the probe's solid-state emission because it will offer a handy approach for practical and on-site applications. We proceeded with **TCNA** as it was selectively and

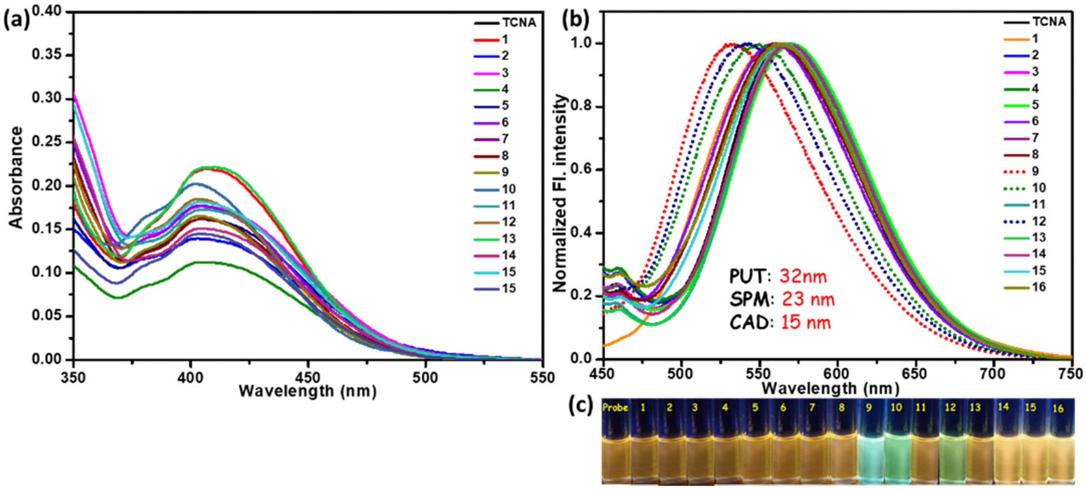

Fig. 2 The (a) absorption spectra and (b) emission spectra of the probe **TCNA** (10 μM in dioxane) after adding various amines (10 μM in DMAc). λ_{ex} = 404 nm; 1-ammonia; 2-aniline; 3-butylamine; 4-diphenylamine; 5-triphenylamine; 6-triethylamine; 7-ethylenediamine; 8-1,3-DAP; 9-PUT; 10-CAD; 11-1,6-diaminohexane; 12-SPM; 13-spermine; 14-*N*-ethyldiisopropylamine; 15-2-phenylethylamine; 16-tryptamine.

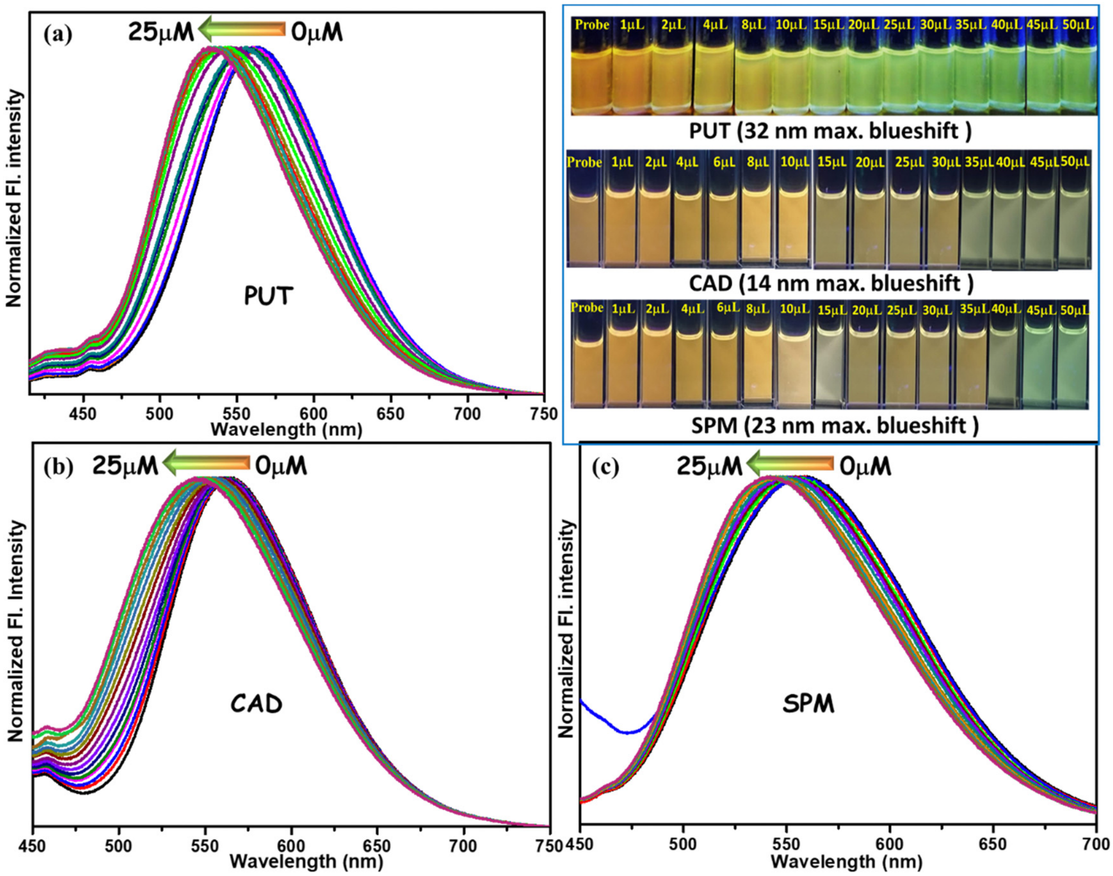

Fig. 3 FL spectra of **TCNA** [10 μM in 1,4-dioxane] upon gradual addition of (a) PUT (b) CAD (c) SPM solution (10^{-6} M), with different volumes (in μL). λ_{ex} = 406 nm. Top of Fig. (c) blue-shifted emission change upon gradually adding PUT, CAD, and SPM (images taken under 365 nm UV-lamp).

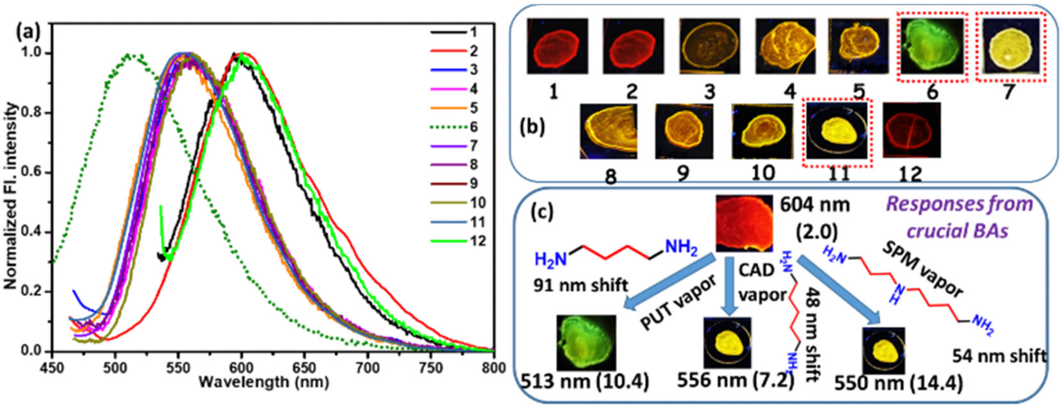

Fig. 4 (a) Normalized FL spectra of **TCNA** thin film before and after exposure to different amine vapors (λ_{ex}: 524 nm for probe; 437 nm after exposure to amine vapor) (b) emission color change (taken under 365 nm UV lamp) in the thin film state 1: **TCNA** after exposure to 2: ammonia; 3: butylamine; 4: ethylenediamine; 5: 1,3-DAP; 6: PUT; 7: CAD; 8: 1,6-diamino hexane; 9: 2-phenylethylamine; 10: *N*-ethyl diisopropylamine; 11: SPM; 12: spermine; (c) selective BAs show the responses: emission λ_{max} and Φ_f (%) are stated in parenthesis.

rapidly reactive with three essential BAs. Although the compound **TCNA** was AIE-inactive, it displays perceptible red emission (λ_{max} = 604 nm, absolute Φ_f = 2%) in the crystalline state. Multiple twisted sites in the probe and numerous supramolecular interactions offer only weak intermolecular $\pi\cdots\pi$ interactions, leading to its behavior as a solid-state emitter (detailed crystal structure/packing: *vide infra*). Strong hydrogen bonding and multiple intermolecular interactions in the crystal lattice classically generate the red-shifted emission with reduced quantum yield. To expose amine vapor to these solid-emitting probes, a thin film on a glass platform would be the most convenient to handle. Therefore, a thin film was prepared by dropping the

TCNA solution (1 mM in 1,4-dioxane) on a glass coverslip and subsequent evaporation to dryness at 25 °C. The red emissive thin film was exposed separately to these three BA vapors (Fig. 4c). A unique and quick blueshift of 91 nm (red to green) was observed after exposure to PUT vapor, whereas 48 and 54 nm blueshift (red to yellow) were observed in the thin film emission with CAD and SPM vapor, respectively (Fig. 4c). Interestingly, the solid-state fluorescence intensity [absolute Φ_f (%)] was significantly improved in all cases after the amine exposures (Fig. 4c). This result looks unique for PUT with an appreciable blueshift compared to the other two BAs, and the reasons are elucidated with evidence.

Concentration-variation emission studies

The above outcomes on abrupt emission shift motivated us to investigate concentration-based emission variation under the vapor phase. At the outset, the probe (1 mM) was drop cast on a silica gel-coated Al-plate and fixed at the wall of the 200 mL glass jar [Fig. 5a (under ambient light)], closed tightly with a rubber septum, and properly enclosed with Teflon tape (Fig. 5a). Six such jars were made ready for the screening and PUT liquid was added through the septum in different μL volumes (5, 7, 12, 30, and 40, Fig. 5b) using a Hamiltonian microsyringe, and the jar was kept at 25 °C. While monitoring the color change using a 365 nm UV lamp, emission changes from red to (i) orange (for 5 μL), (ii) orange-yellow (for 7 μL), (iii) yellow (for 12 μL), and finally (iv) cyan (for both 30 and 40 μL) were identified.

As stated before, the vapor pressure (at 25 °C) of PUT and CAD are different, *i.e.*, 2.3 mm Hg and 0.921 mm Hg, respectively. Also, the boiling point of PUT is lower (159 °C) than CAD (179 °C); thus, the evaporation process of PUT is much more favorable than CAD. Again, inside the closed jar, PUT vapor touches the fluorescent dye and reacts to form salt. Therefore, PUT vapor will continue reacting with the dye until it reaches the vapor–liquid equilibrium in the closed jar. During this process, the degree of various interactions between the fluorophore and PUT molecules will be altered, resulting in emission variation. Hence, after reaching equilibrium at a specific concentration, emission remains unchanged even after increasing the amount of PUT.

Such diverse emissions at different concentrations were further investigated spectroscopically; therefore, we repeated the same experiment with a clean **TCNA**-drop-casted glass coverslip (1 mM in 1,4-dioxane). The red-emissive coverslip was affixed inside the wall of the glass jar (volume of 200 mL). The glass jar was sealed with a septum and Teflon tape (Fig. 5a and b). The emission color change of the fixed coverslip was monitored using a 365 nm UV lamp. Different volumes of PUT were added to the bottom of the sealed chamber at 25 °C. Although the emission color change was rapid and visually detectable, the emission spectra (Fig. 6a) were recorded after 10 min. The observed emission shift slightly differs between silica gel-coated Al-plates and glass surfaces, being a chemically different entity.

The PUT liquid [1 μL (4.43 mg L^{-1})] was added precisely and found an instant 28 nm blue-shifted emission from red (λ_{max}= 604 nm) to yellowish orange (λ_{max}= 576 nm) along with an enhancement in Φ_f (%) [see Table S4 and Fig. 5c]. Gradually, the experiment was performed with different amine concentrations by increasing the amount of PUT. The red emissive film became yellow with a blueshift of 52 nm with 1.7 times enhancement in Φ_f (%). All these emission variations are rapid (within 10 s), and even the shifts remain intact till the next PUT addition. When the volume of PUT was increased to 15 μL, there was a 73 nm blueshift with a greenish emission with almost unaffected Φ_f (%). Still, on further increasing of PUT amount [20, 25 or 30 μL], an overall 91 nm blue-shifted emission [513 nm, green] was noticed along with impressive heightening in the Φ_f (%) from ~3 to ~10. Further, the sensitivity of **TCNA** was tested by repeating the same experiment with 2 μL of PUT in a 6 L closed jar, and a 28 nm blue-shifted emission was detected [red to

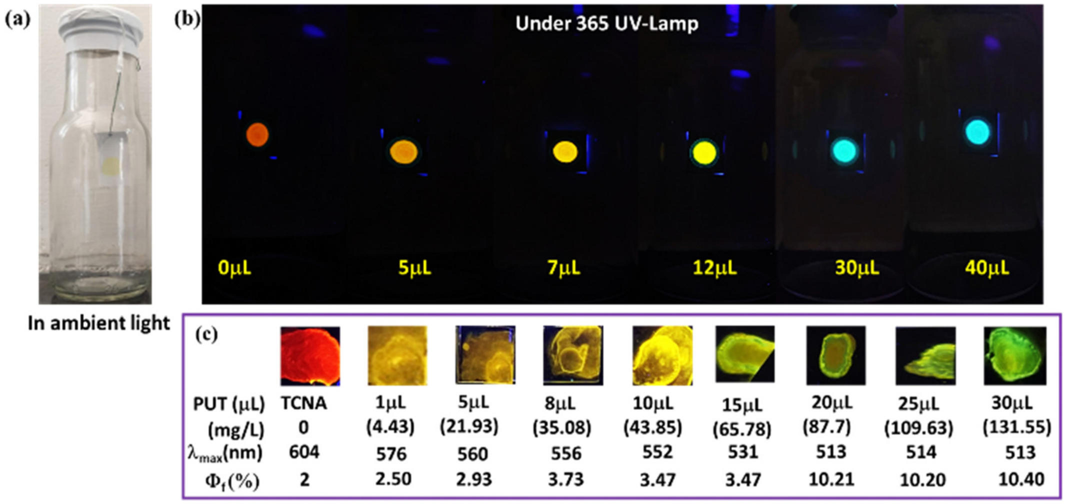

PUT (μL)	TCNA	1μL	5μL	8μL	10μL	15μL	20μL	25μL	30μL
(mg/L)	0	(4.43)	(21.93)	(35.08)	(43.85)	(65.78)	(87.7)	(109.63)	(131.55)
λ_{max}(nm)	604	576	560	556	552	531	513	514	513
Φ_f(%)	2	2.50	2.93	3.73	3.47	3.47	10.21	10.20	10.40

Fig. 5 (a) The probe drop-casted on silica gel-coated Al-plate (under ambient light); (b) the images of drop-casted silica gel-coated Al-plates are taken under a 365 nm UV lamp at different concentrations (μM) of PUT liquid [0, 49.7, 248, 398, 497, 746, 994, 1243.6 and 1490]. (c) Concentration-tuned emission using the probe drop-casted on a coverslip.

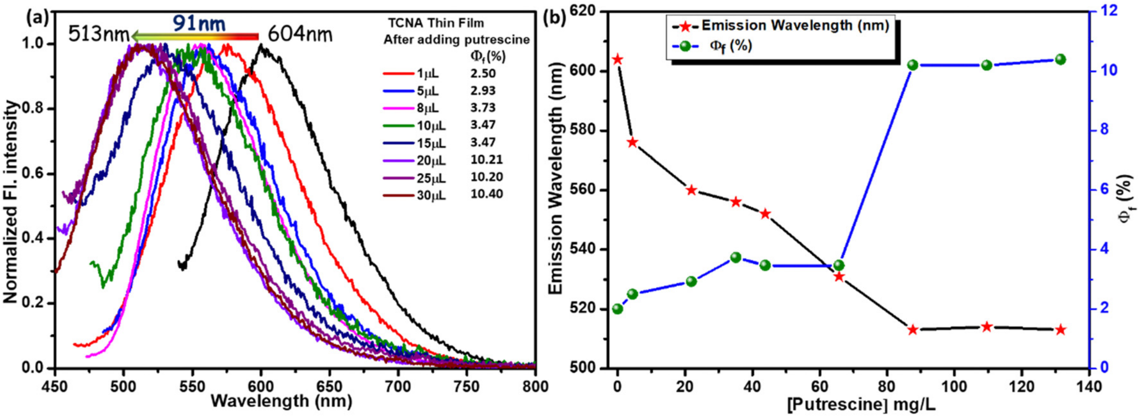

Fig. 6 (a) Emission spectra for all the coverslips at different PUT concentrations. (b) a plot of emission wavelength (nm) and absolute Φ_f (%) with [PUT] (mg L^{-1}).

yellowish orange; Fig. S13A, ESI†], which further validates the PUT vapor detection at a much lower concentration as low as 3.3 μM. Hence, wavelength shift and quantum yield with PUT concentration are summarized in Fig. 6b. While performing the same concentration-tuned emission studies with SPM and CAD, the red emissive film was converted to yellow [only 54 nm and 49 nm blueshift for SPM and CAD, respectively, Fig. S13B (ESI†); for other related data, spectra, and plots, see Fig. S14 and Tables S5, S6, ESI†]. Unlike PUT, we hardly find any additional variations from the yellow emissive state for SPM and CAD, even after adding excess (30 μL) amines. This result also dictates that SPM is considerably less responsive than CAD because of the much lower vapor pressure for SPM. Notably, Φ_f (%) was significantly higher (14.4) for SPM than CAD (7.4). The green coloration results from the direct touch of PUT liquid and vapor, while CAD and SPM demonstrate only yellow emission. Thus, this probe is unique in recognizing PUT compared to other common BAs such as SPM and CAD.

Mechanistic insight for the concentration-guided emission

We attempted to find the mechanistic viewpoint on how the probe, **TCNA**, interacts with such specific BAs. It assists in interpreting selective and sensitive concentration-based detection of PUT. Although CAD and SPM responded significantly, the concentration-based variation was prominent only with PUT due to its slightly higher basicity and decent vapor pressure than CAD and SPM.[13,49] However, the carboxylic acid functionality would immediately form an ammonium carboxylate salt, changing the overall molecular electronic distribution within **TCNA**. A rapid formation of ammonium salt, *i.e.*, **TCNASA** [no intramolecular proton exchange (IPE)] or **TCNASB** [with IPE], consisting of supramolecular interactions, is anticipated at 25 °C (Fig. 7).

Experimental and theoretical studies were conducted to support this **TCNAS** formation. Firstly, ammonium carboxylate salt formation is recognized upon slow exposure of PUT vapor as obtained from FT-IR studies (Fig. S15a, ESI†) that depict a broad envelope at 3750–2750 cm^{-1} with the disappearance of the O–H stretching (cm^{-1}) at ∼3641 & 3067–2855 for pure **TCNA**. Subsequently, the appearance of a broad peak at 3413 cm^{-1} and merged stretching (cm^{-1}) at ∼1600 and 1500 (NH bending vibration) designate the presence of an $-NH_3^+$ unit.[50a] Moreover, the vanishing of intense C=O stretching (cm^{-1}) at

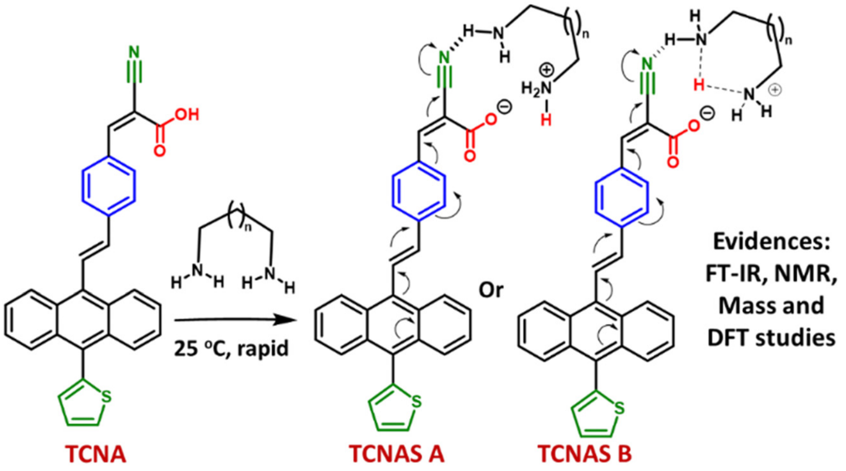

Fig. 7 Plausible mechanism for the interactions between TCNA and the selected BAs.

1700, followed by the arrival of two bands at 1630–1567, further confirms the formation of a negatively charged carboxylate ion (Fig. S15a, ESI†).[50b] Next, we attempted to locate the $-\mathrm{C}{\equiv}\mathrm{N}$ stretching to validate the presence of $-\mathrm{C}{\equiv}\mathrm{N}\cdots\mathrm{H}$ interactions. However, strong-electronic conjugations of **TCNA** offer a very weak $-\mathrm{C}{\equiv}\mathrm{N}$ stretching at 2223 cm^{-1},[51] gradually weakening with a 12 cm^{-1} shift due to the lowering of force constant. Lastly, we could notice a broad signature at $\sim$2142 cm^{-1} for **TCNAG** (TCNA-Green form), which could be attributed to the presence of the $-\mathrm{C}{\equiv}\mathrm{N}\cdots\mathrm{H}$ motif and other merged combination bands. The electron-withdrawing properties of the carboxylic acid group will be lost after turning into an ammonium carboxylate. Thus, the π-electron delocalization will end mainly in the cyano group, developing intermolecular $-\mathrm{C}{\equiv}\mathrm{N}\cdots\mathrm{H}$ interactions. Notably, accumulated negative charge on nitrogen will enable the resonance-affected H-bonding, as reported after analyzing several amino and cyano-based systems.[52] The linear cyano group can also act as an H-bond acceptor by simultaneously interacting with two amine groups.[53] However, such possibilities may not effectively operate in this system as the dicyano compound **TCN** was inactive in recognizing the diamines. Next, ^{1}H-NMR-spectrum reveals the disappearance of carboxyl proton from **TCNA** (Fig. S16A-a, ESI†) after titrating with PUT, further justifying the salt formation. There is a slight upfield shift of $\sim\delta$ 0.1 in *trans*-olefinic protons (J = 16.0 Hz) of **TCNA**, the closest part of the reactive center (Fig. S16A-b, ESI†), demonstrating the marginal enhancement of electron density around those protons after the amine treatment. Moreover, one proton will undergo intramolecular exchange to form a stable cyclic complex **TCNASB**, which is still eligible for $-\mathrm{C}{\equiv}\mathrm{N}\cdots\mathrm{H}$ interactions. However, we attempted to locate the change in the ^{13}C-NMR signal for $-\mathrm{C}{\equiv}\mathrm{N}$ to recognize $-\mathrm{C}{\equiv}\mathrm{N}\cdots\mathrm{H}$ interactions, but the lack of solubility became detrimental in identifying the difference. However, no product from Michael-type addition was indicated in the ^{1}H NMR spectrum.

Nevertheless, gradual salt formation followed by the $-\mathrm{C}{\equiv}\mathrm{N}\cdots\mathrm{H}$ interactions would stabilize the overall entities. Therefore, we were interested in finding the stepwise changes in each wide-angle X-ray scattering (WAXS) pattern (Fig. 8).

Few distinct diffractions of the probe **TCNA** could be identified before exposing PUT. A slight exposure demonstrates changes in the WAXS pattern where a few diffractions appeared and a few disappeared. However, the intensity of the diffracted signals is enhanced in the **TCNAO** (orange) sample with slightly higher interplanar distances. On further concentration-enhancement of the PUT vapor, the yellow emitting solid **TCNAY** displayed only a few diffractions (mostly broad). Notably, the sample appeared as a slightly gummy solid (different texture in SEM) at this stage, which could be the origin of such a broader diffraction pattern. However, the green emitting **TCNAG** shows a well-diffracted WAXS pattern, indicating a higher crystallinity and symmetry development in the sample due to the salt formation and generation of the $-\mathrm{C}{\equiv}\mathrm{N}\cdots\mathrm{H}$ complex. Thus, the molecule tends stepwise to transform to a more crystalline phase upon diamine fuming. The amine vapor instantly reacts with the acid probe, and liquid–vapor equilibrium is accelerated by enhancing the concentration of amine vapor. All these experimental findings confirm the requirement of diamines and address how concentration variation gradually changes the molecular arrangement, contributing to emission switching. To get better insight into the morphological transitions of all the forms of **TCNA** after exposing PUT vapor, scanning electron microscopic (SEM) images were captured (Fig. S15b, ESI†). It clearly specifies the morphological differences in various emissive forms. **TCNA** mainly shows an aggregated semi-crystalline state for the probe, which is gradually distributed in **TCNAY**, and finally, there is a development in crystallinity with **TCNAG**. This result is in agreement with the WAXS pattern discussed above.

All these deviations in IR/NMR, SEM images, and WAXS patterns of **TCNA** after exposing PUT vapor are primarily

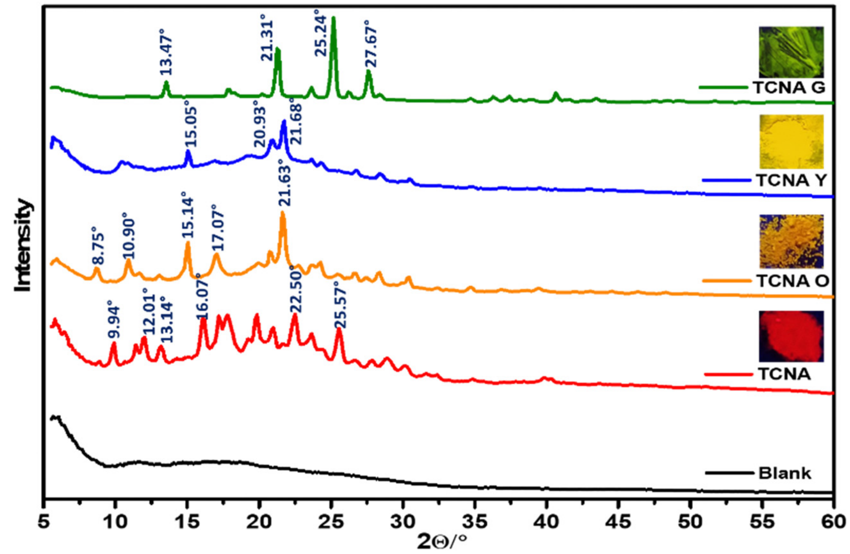

Fig. 8 Changes in the WAXS pattern at different emissions (images are taken under a 365 nm UV-lamp).

accountable for the observed outcomes. Moreover, all these variations display a variance in the ground state, showing a difference in the absorption spectra (Fig. S17, ESI†). The UV absorption of **TCNA** solid indicates a red dye ($\lambda_{\max}$ = 532 nm), which shifted to 438 nm (yellow solid, 94 nm blueshift) for **TCNAY** after exposure to PUT vapor. Finally, **TCNAG** displayed the absorption $\lambda_{\max}$ at 420 nm (yellowish green, overall 112 nm blueshift in solid state absorption spectra). It designates that the changes in ambient light are also visually promising and easily detectable. Further, LC-MS studies (in the negative ion mode, Fig. S18, ESI†) prove the existence of **TCNASB**, which appeared with a peak at 543 $[\mathrm{M-2H}]^-$ along with the molecular ion peak at 456 $[\mathrm{M-H}]^-$.

In addition, a few more control experiments were performed to establish the mechanistic insights. A few molecules, such as 4-aminobutanol, *N*,*N*-dimethylbutane-1,4-diamine and lysine (acting as bases and H-bond acceptors), were treated with the **TCNA** solution. In the solution state, no significant change in the emission has been observed (Fig. S19, ESI†) because 4-aminobutanol would possibly prefer forming intra/intermolecular H-bonding, and the interactions between these amine analytes and **TCNA** solution are not impressive. Further, the solid probe was treated with these liquid amines to investigate the response in the vapor phase. Although these liquids have much higher boiling points (°C) [206 for 4-aminobutanol and 181 for *N*,*N*-dimethylbutane-1,4-diamine] and lower vapor pressure (at 25 °C) than PUT, we attempted with these liquid amines (30 μL) inside a closed 200 mL jar. Both 4-aminobutanol and *N*,*N*-dimethylbutane-1,4-diamine responded in the vapor phase (Fig. S20, ESI†), resulting in a yellow emissive solid. Notably, diamine showed a better response with a 44 nm shift. Thus, vapor can interact better after getting trapped inside the layer of a solid-emissive probe. Still, unlike other amines, PUT exhibits the unique green emission. Thus, these molecules are interesting to investigate regarding the emission features, particularly the vapor concentration-based emission change. The difference in vapor pressure, basicity, and boiling point of these amines compared to PUT creates the interaction variation.

To further validate the proposed H-bonding between $-\mathrm{C{\equiv}N\cdots H}$, the emission shift was studied by experimenting with an H-bonding competing solvent, such as MeOH (Fig. S21, ESI†). A 32 nm blue-shifted emission was noticed in a 1,4-dioxane solution of **TCNA** after adding PUT. However, the shift was reduced to only 23 nm in the presence of 10% MeOH in 1,4-dioxane (Fig S21, ESI†). In addition, the polarity enhancement reduced the emission intensity, as expected. We speculate that the presence of MeOH restricts the $-\mathrm{C{\equiv}N\cdots H}$ interactions within the dye and PUT unit in the solution state and, therefore, makes a barrier to bring a green emission.

Explanation with single crystal X-ray structure/molecular packing

To decipher a detailed view of the crystal lattice, we determined the crystal structure and molecular packing of the compound **TCNA**, driven by various intermolecular interactions listed in ESI† (Fig. 9b and Fig. S22, S23, Tables S7, S8, ESI†). Two symmetrically independent molecules are in an asymmetric unit with multiple twists (Fig. 9a). Such a twisted structure prevents strong $\pi\cdots\pi$ interactions [the centroid distances (Å) are within the range of 4.77, 8.54, and 11.53, Fig. S22b, ESI†], resulting in an emissive solid. In addition, multiple supramolecular interactions such as acid dimerization and $-\mathrm{C{\equiv}N\cdots H}$ interactions holding diverse directionalities could be responsible for reducing the overall quantum yield. A strong intermolecular H-bonding appeared with a distance of 1.75–1.79 Å and a bond angle of ~176° (Fig. 9b). The $-\mathrm{C{\equiv}N}$ distance of 1.150 Å specifies the presence of conjugations.[50] However, weaker $-\mathrm{C{\equiv}N\cdots H}$ interactions are noticed in the crystal within the distance range of 2.6–2.7 Å, and nonlinear bond angles of $-\mathrm{C{\equiv}N\cdots H}$ make these existing interactions much more vulnerable (Fig. 9b and Fig. S22a, ESI†). Even after several attempts, a suitable single crystal of **TCNA-PUT** complex could not be generated after the PUT exposure, possibly because of PUT's instability (hygroscopic and tendency to react with O_2, CO_2) in the air.

The blue-shifted emission can be described as the relative reduction of conjugation in **TCNAS**. Moreover, the $-\mathrm{C{\equiv}N}$ unit prefers a slightly tilted conformation rather than a linear site.[53,54] After the generation of the $-\mathrm{C{\equiv}N\cdots H}$ system, the overall conjugation in the system is significantly reduced, and therefore, a 91 nm blueshift in emission appeared. Thus, the system becomes more twisted, which prevents $\pi\cdots\pi$ stackings and leads to a radiative decay. The enhancement in the quantum yield can be attributed to the well-known crystallization-induced emission enhancement effect (CIEE).[55–57] Upon PUT

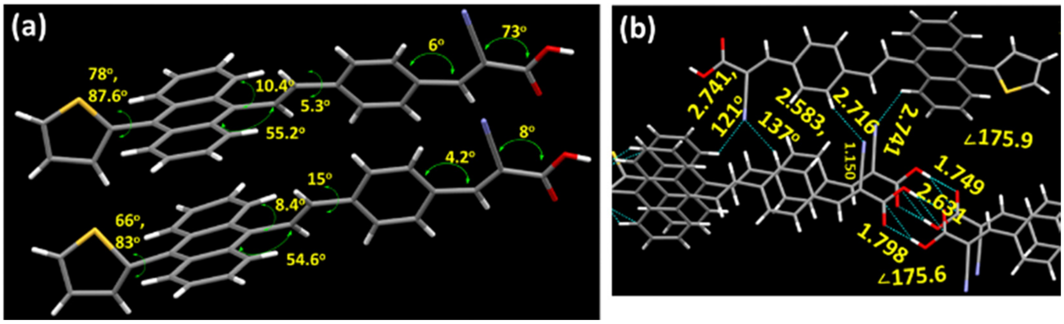

Fig. 9 (a) Single-crystal X-ray structures with few selected bond angles (°), (b) partial molecular packing of **TCNA** with few significant noncovalent interaction distances (Å) and angles (°) (further details: see Fig. S22a and S23a, ESI†).

fuming, the molecule experiences a few weaker supramolecular interactions, enabling the rigidification of the molecular structure and blocking the non-radiative decay.

Further, the selective and sensitive gradual detection of PUT can be supported with the void space available (367 Å^3 obtained from Mercury; Fig. S23b, ESI†) in the crystal lattice of **TCNA**. The PUT vapor can be easily trapped in the space available and produce the ammonium carboxylate salt that offers successive intramolecular proton exchange/$-C\equiv N\cdots H$ interactions. Close contact in a confined system would desire gradual and effective interactions. Thus, the available void space and the carboxylic acid group can help interactions for most of the amines exposed in the solid state and display emission shift. However, monoamine would not have any scope for further proton exchange and, therefore, can be differentiated. Unlike solution states, ethylene–diamine and 1,3-DAP can interact similarly to other BAs. However, the emission shifts and quantum yield enhancements were not impressive.

Reversibility nature

The reusable fluorophores to detect BAs are hardly established in this field because the fluorophores mostly react with the BAs, and therefore, returning to the original state is problematic. After realizing the possible perception, we expected the reversibility nature of the probe in the presence of acid. The acid (HCl) fumes can destroy the salt and other interactions, enabling it to return to the initial stage for further use. We have conducted the reversibility experiment and identified the visually detected color changes for the 6th time with intact emission quantum yield, as presented in Fig. S24 (ESI†). Thus, we have established this probe as a reusable platform for practical applications.

Theoretical investigation

To attain further rationalization on our thought of **TCNA-PUT** interactions, optimized molecular structures of **TCNA** and **TCNA-PUT** were determined using DFT (density functional theory)/TD (time-dependent)-DFT studies using CAM-B3LYP[58] functional and 6-31+G(d) basis set. The calculated absorption and emission λ_{max} match well with the experimentally observed results. The theoretically optimized structures (Fig. 10 and Table S9, ESI†) of individual species displayed a significant difference in the bond lengths (Å)/angles (°) compared to **TCNA** crystal, as expected. **TCNA** shows a linear $-C\equiv N$ functionality with a bond length of 1.164 with a $-C-C\equiv N$ angle of 177 (almost linear, Fig. S25A, ESI†). Nevertheless, the **TCNA-PUT** complex offers the transfer of the acidic proton of amine nitrogen (bond length 1.753 Å), and a subsequent intramolecular proton exchange between two amine functionalities *via* forming a stable cyclic complex **TCNASB** (Fig. 10) was noticed, as discussed earlier in Fig. 7.

The related bond/interatomic distances and angles (Fig. 10) would support this intramolecular proton exchange. The enhancement in the $-C\equiv N$ bond length (1.168 Å) was noted due to $-C\equiv N\cdots H$ interaction (2.373 Å). It is pertinent to mention that the $-C\equiv N\cdots H$ interaction in the molecular crystal packing of **TCNA** lies between 2.583–2.741 Å, representing much stronger interactions between the amine NH and $-C\equiv N$ functionality in the gaseous state. These calculations validate our mechanistic assumption on the selectivity of diamines. The nitrile group also became nonlinear after the interactions with diamines, and the slight change in the dihedral angle also reduced the electronic π-conjugation, responsible for the blueshift.

Further, to understand the deviation with smaller amines such as 1,3-DAP, we focused on the **TCNA-1,3-DAP** interactions, and therefore, the molecular geometry was optimized (Fig. 10b). It primarily disclosed two notable differences that include a strong salt formation with 1,3-DAP (being a relatively stronger base) and weak hydrogen exchange between the two amine groups because of the non-preferable $\angle NH\cdots N$ 136° angle and longer $N-H\cdots N$ interatomic distance 1.961 Å compared to **TCNA-PUT** system (Fig. 10a). Moreover, $-C\equiv N\cdots H$ interaction is weaker in 1,3-DAP, as validated with a relatively larger interatomic distance of 2.392 Å (2.373 Å for **TCNA-PUT**). Thus, the other $-NH_2$ functionality of DAP was relatively more accessible, which could be the reason for being nonresponsive in solution state emission. However, these groups will be confined to the solid state and display an emission shift.

Further, the highest-occupied molecular orbital (HOMO) of **TCNA** is mainly built up with an anthracene core. At the same time, the lowest unoccupied molecular orbital (LUMO) is occupied by the cyano/acid attached ring (Fig. S26, ESI†). The **PUT-TCNA** complexes do not change the HOMO significantly, but the LUMO formation differs due to the carboxylate formation, which enhances electron density. Thus, LUMO is destabilized by ∼0.9 eV, leading to the blueshift (Table S9, ESI†).

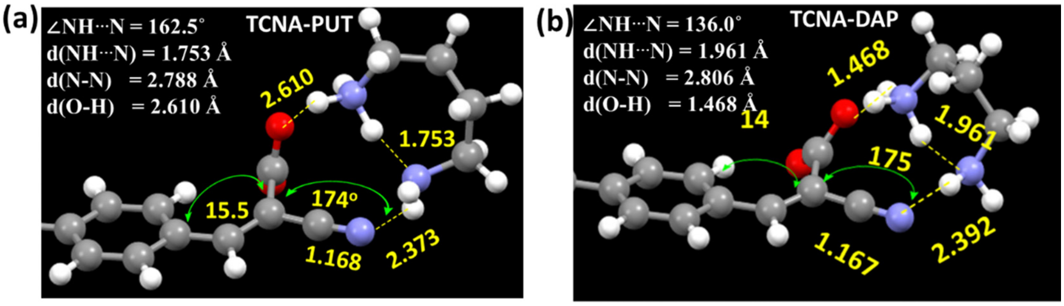

Fig. 10 Optimized molecular structure (gaseous state) of (a) **TCNASB**: TCNA-PUT and (b) TCNA-1,3-DAP with selected angles (°) and interatomic distances/bond length (Å). (Partial structure is shown here for clarity; For further details, see Fig. S22B, ESI†).

Detection of the freshness of fish and chicken

The remarkable blue-shifted emission and sensitivity, specifically towards PUT (a vital marker for detection of food's freshness) in the vapor phase, have encouraged us to monitor the freshness of market-available fresh fish and chicken samples (on a small scale). The probe was drop cast on a Whatman filter paper (cheapest and easiest to introduce), fixed inside the glass jar containing the fish/chicken sample, and sealed with a rubber septum, and an empty jar was used as a control to monitor the changes (see Fig. 11). The emission change was surveyed under a 365 nm UV lamp with different time intervals. A slight emission shift was observed after 5 h for fish; however, the difference was intensified after 7 h for chicken. The change would be more promising if a large sample scale is tested within a small period.

The orange emissive filter paper became yellow after 22 h, whereas the control spot remained unchanged. The same experiment was also performed with a piece of fish pellet, and a similar change was noticed after 5 h (Fig. 11). In the case of the fresh chicken sample, the emission started changing within 7 h (a little slower in forming BAs vapor). After 22 h, the change was detectable. The direct touch of spoiled chicken could also be identified with its rapid emission change from red to green. Thus, the quick and distinct emission color change using **TCNA** has been successfully established to detect fish/chicken freshness using an inexpensive strategy.

Experimental

Materials and general conditions

All the chemicals were purchased from Merck, and the solvents for column chromatography were purchased from Finar. Spectroscopic grade solvents used for UV-Vis and fluorescence spectroscopy were purchased from Finar. All the photophysical studies were performed at room temperature, 298 ± 2 K. ^{1}H, and ^{13}C NMR spectra were recorded on Bruker 400 MHz spectrometers with operating frequencies of 101 MHz for ^{13}C. Chemical shifts (δ) are reported in ppm relative to the residual solvent signal (δ 2.50, δ 7.26 for ^{1}H NMR and δ 39.5, δ 77.0 for ^{13}C NMR).

Synthesis and characterizations

Diethyl ((10-(thiophen-2-yl)anthracen-9-yl)methyl)phosphonate[37]**.** This compound was synthesized following earlier reported methods. ^{1}H NMR (400 MHz, CDCl$_3$) δ 8.41 (d, J = 8.9 Hz, 2H), 7.89 (d, J = 8.8 Hz, 2H), 7.63–7.54 (m, 3H), 7.42 (dd, J = 8.7, 6.5 Hz, 2H), 7.31 (dd, J = 5.2, 3.4 Hz, 1H), 7.19 (m, 1H), 4.29 (d, J = 22.5 Hz, 2H), 4.08–3.83 (m, 4H), 1.17 (t, J = 7.1 Hz, 6H).

Synthesis of (*E*)-4-(2-(10-(thiophen-2-yl)anthracen-9-yl)vinyl)-benzaldehyde (TAA). In a 50 mL round-bottomed flask, diethyl ((10-(thiophen-2-yl)anthracen-9-yl)methyl)phosphonate (0.20 g, 0.487 mmol) was dissolved in 10 mL of dry DMF under nitrogen atmosphere at 25 °C followed by the addition of NaH dispersed in 60% paraffin oil (0.093 g, 3.4 mmol) in the reaction mixture at 0 °C and stirred for 10 min. Terephthaldehyde (0.130 g, 1.21 mmol) was added slowly to the solution. The reaction was allowed to stir for 1 h, and TLC monitored the completion of the reaction. The resulting reaction mixture was quenched using water, extracted with ethyl acetate (20 mL × 3), dried over anhydrous sodium sulfate, and concentrated using a rotary evaporator. The compound **TAA** was purified using column chromatography (100–200 mesh-sized silica gel) using petroleum ether to obtain a yellow solid.

TAA. Yield 50% (0.097 g), m.p. 205–210 °C, IR (ν cm^{-1}, in KBr): 2920, 1689, 1596, 1564, 1438, 1373, 1256, 1211, 1164, 1025, 973. ^{1}H NMR (400 MHz, CDCl$_3$) δ 9.99 (s, 1H), 8.28–8.26 (m, 2H), 8.06 (d, J = 16.8 Hz, 1H), 7.91–7.89 (m, 2H), 7.82–7.75 (m, 4H), 7.56–7.54 (m, 1H), 7.43–7.33 (m, 4H), 7.25–7.23 (m, 1H), 7.13–7.12 (m, 1H), 6.96 (d, J = 16.8 Hz, 1H). ^{13}C NMR (101 MHz, CDCl$_3$) δ 191.7, 143.04, 139.01, 136.6, 135.8, 133.3, 131.7, 130.4, 129.5, 129.2, 128.8, 127.2, 127.1, 126.8, 125.7, 125.6. HR-MS for $C_{27}H_{19}OS$, calc. 391.1157, found 391.1136.

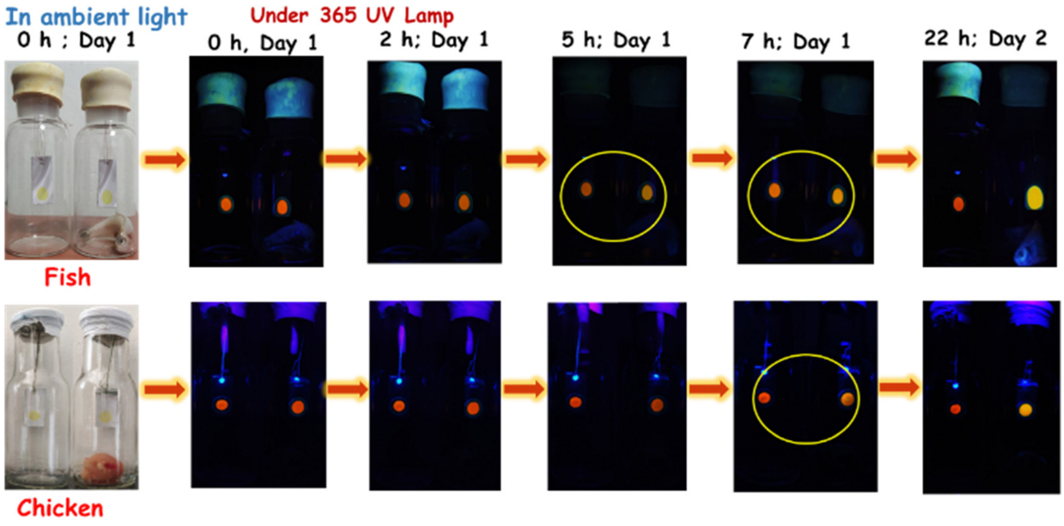

Fig. 11 Application of the probe in detecting the freshness of fish and chicken.

Synthesis of (*E*)-2-(4-(2-(10-(thiophen-2-yl)anthracen-9-yl)vinyl)-benzylidene)malononitrile (TCN). In a 50 mL round-bottom flask, (*E*)-4-(2-(10-(thiophen-2-yl)anthracen-9-yl)vinyl)benzaldehyde (0.20 g, 0.51 mmol) and malononitrile (0.067 g, 1.02 mmol) were dissolved in 20 mL of ethanol–water mixture (6 : 1) at room temperature. The reaction mixture was heated to reflux for 7 hours at 80 °C. The reaction was monitored by TLC. Upon completion, the reaction mixture was allowed to cool to room temperature. The resulting precipitate was washed with cold ethanol and dried under a high vacuum to obtain an orange solid.

TCN. Yield 70% (0.160 g), m.p. 250–253 °C, IR (ν cm^{-1}, in KBr): 2223, 1538, 1549, 1468, 1417, 1377, 1221, 1184, 1028, 970. ^{1}H NMR (400 MHz, $CDCl_3$) δ 8.25 (d, J = 8.8 Hz, 2H), 8.14–8.08 (m, 1H), 7.95–7.93 (m, 2H), 7.82–7.80 (m, 2H), 7.77–7.72 (m, 3H), 7.56–7.55 (m, 1H), 7.44–7.34 (m, 4H), 7.26–7.23 (m, 1H), 7.13–7.12 (m, 1H), 6.96 (d, J = 16.8 Hz, 1H). ^{13}C NMR (101 MHz, $CDCl_3$) δ 154.1, 138.6, 134.1, 131.3, 128.09, 126.9, 126.8, 125.6, 125.2, 124.8, 124.4, 122.8, 122.5, 122.1, 121.04, 109.2, 108.1, 77.2. HR-MS for $C_{30}H_{19}N_2S$, calc. 439.1269, found 439.1258.

Synthesis of (*E*)-2-cyano-3-(4-((*E*)-2-(10-(thiophen-2-yl)anthracen-9-yl)vinyl)phenyl)acrylic acid (TCNA). In a 50 mL round-bottomed flask, (*E*)-4-(2-(10-(thiophen-2-yl)anthracen-9-yl)vinyl)-benzaldehyde (0.20 g, 0.51 mmol) and cyanoacetic acid (0.130 g, 1.53 mmol) was dissolved in 20 mL of chloroform under nitrogen atmosphere at room temperature. Piperidine (0.3 mL, 3.07 mmol) was added, and the reaction mixture was heated to reflux for 24 hours at 62 °C. The completion of the reaction was monitored by TLC. The resulting reaction mixture was quenched using water, extracted with ethyl acetate (20 mL × 3), dried over anhydrous sodium sulfate, and concentrated using a rotary evaporator. The compound **TCNA** was purified using column chromatography (100–200 mesh-sized silica gel) using 50% ethylacetate-hexane to obtain a red solid. The single crystals are grown from a mixture of dimethylsulfoxide (DMSO)/CH_3CN (9 : 1).

TCNA. Yield 90% (0.211 g), m.p. 179–181 °C, IR (ν cm^{-1}, in KBr): 3614, 3067, 2922, 2855, 2264, 2223, 1700, 1582, 1418, 1270. ^{1}H NMR (400 MHz, DMSO-d_6) δ 13.60 (s, 1H), 8.50–8.43 (m, 4H), 8.22–8.20 (m, 2H), 8.12–8.10 (m, 2H), 7.98–7.97 (d, J = 4.8 Hz, 5H), 7.83–7.81 (m, 2H), 7.64–7.56 (m, 4H), 7.46–7.44 (m, 1H), 7.34–7.33 (m, 1H), 7.14 (d, J = 20 Hz, 1H). ^{13}C NMR (101 MHz, DMSO-d_6) δ 166.2, 163.8, 153.8, 141.7, 138.42, 137.04, 134.2, 131.7, 131.4, 130.3, 129.09, 128.6, 128.3, 128.2, 128.02, 126.7, 126.4, 126.3, 116.9, 116.1, 104.02. HR-MS for $C_{30}H_{20}NO_2S$, calc. 458.1215, found 458.1219. X-ray structure was determined for this compound. CCDC No: 2262179.†

Single crystal measurement

All measurements were carried out using a Rigaku XtaLAB P200 diffractometer using multi-layer mirror monochromated Cu-Kα radiation (λ = 1.54184 Å). The measurements were taken at a temperature of −173 ± 1 1 °C up to a maximum 2θ value of 149.81°. CrysAlisPro was used to collect and process data (Rigaku Oxford Diffraction). Cu-Kα radiation has a linear absorption coefficient, μ, of 18.391 cm^{-1}. The transmission factors ranged from 0.227 to 0.593 when an empirical absorption correction was implemented. The data were corrected for the Lorentz and polarization effects. The structure was solved using direct methods (SIR2011)31 and expanded using Fourier techniques. The non-hydrogen atoms were refined anisotropically. Hydrogen atoms were purified using the riding model. All calculations were performed using the Olex2 crystallographic software package except for the refinement, which was performed using SHELXL Version 2014/7.

WAXS measurement

WAXS measurements were carried out using a Xenocs Nano-inXider SW-L SAXS/WAXS system with a dual detector with Cu Kα micro focus within the range of 5° to 60° at a scanning speed of 2° min^{-1}. The sample was placed and spread over a Kapton tape, and data were recorded in transmission geometry. The results are presented after background subtraction using xenoc XSACT software for all the samples.

Methods and measurements

All the fluorophores were synthesized using a method reported earlier. The electronic absorption spectra were recorded with UV 3600 Plus (Shimadzu). The FL spectra were recorded using a Hitachi spectrofluorometer (F7000) using a 1 cm path-length quartz cuvette. Origin Pro 8.5 software is used to plot the obtained data.

Preparation of solutions

The stock solution of 10^{-3} M **TCNA** was prepared in 1,4-dioxane. The 10^{-3} M stock solution for all the amines was prepared in *N*,*N*-dimethylacetamide (DMAc).

Absorption and FL studies

Absorption studies were carried out with the sample (2 mL, 10 μM) in a quartz cuvette (1 cm × 1 cm). The wavelength range was kept within 550 to 200 nm. Emission spectra of the same sample are instantaneously recorded with the range from 415 to 800 nm, with a PMT voltage of 400 eV and excitation slit/emission slit 5.0.

Absolute quantum yield measurement

The solid-state absolute quantum yield measurement used a calibrated integrating sphere method with an absolute error of ±2%.

Time-resolved decay measurement

Solution-state lifetime measurement. The solution-state lifetime was measured with 10 μM 2 mL solution of TCNA *via* pulse excitation of 405 nm followed by the addition of 1 μL, 2 μL (+1 μL), 4 μL (+2 μL), 6 μL (+2 μL), 8 μL (+2 μL), 10 μL (+2 μL), 15 μL (+5 μL) and 20 μL (+2 μL) of PUT (10^{-3} M) solution. The decays for the compound and after the addition of PUT were fitted triexponentially.

Detection limit calculation

A series of fluorometric titrations were conducted to detect the amount of PUT with a 10 μM solution of TCNA.

Study of TCNA coated thin films for visual detection of putrescine

For the thin film study, a 10^{-3} M solution of **TCNA** was drop-cast on thin glass coverslips and dried at room temperature. The dried glass coverslips were affixed on the wall of a 200 mL glass bottle sealed with a septum. Different volumes of putrescine were added, and the observed fluorescence color switching was instantaneous. All the images were taken with a Xiaomi Mi. A3 (*f*/1.8, 1/3, ISO250) after 15 min. Other information is articulated in detail in the ESI.†

Paper strip sensing study

For the solid-state sensing study, a solid TCNA sample was dispersed on strips of Whatman filter paper (15 cm × 4.5 cm) and dropped with different concentrations of putrescine (2 μL) solution in DMAc. The image was taken with a Xiaomi Mi. A3 (*f*/1.8, 1/3, ISO250) after 1 min. However, the blue-shifted emission color change was instantaneous. Other information is articulated in detail in the ESI.†

Theoretical details

The ground state (S_0) geometry of the molecules was optimized using the density functional theoretical (DFT) method with the CAM-B3LYP[56] functional and 6-31+G(d) basis set. After geometry optimization, frequency calculations were done to confirm the absence of any unstable normal modes. The excited state (S_1) calculation uses the TD (time-dependent)-DFT method. All the DFT and TD-DFT calculations were performed using the Gaussian 09 package.[59] All the MOs are visualized in Avogadro software[60] and reported an isosurface value equal to 0.02 a.u.

Conclusions

In conclusion, a suitably designed small molecule with a cyanoacrylic acid opening was realized as a solution and solid-state emitter. Comparative studies with analogous probes revealed that the BAs did not respond toward aldehyde functionality or Michael acceptors introduced in this set of analogs. The TCNA probe could selectively recognize PUT, CAD, and SPM in the solution state, with a higher blue shift for PUT in μM level sensitivity. However, this probe shows its uniqueness with its more glowing blue shift in the solid state for all three amines specifically, while PUT shows a maximum 91 nm shift from red to green. This probe detected PUT vapor concentration (as low as 0.292 mg L^{-1}) with a distinct color change at each level. Further, this probe was repeatedly used for the detection of PUT. Our experimental (FT-IR, NMR) outcomes infer that **TCNA** forms a salt with PUT vapor and gradually turns into a complex through $-C{\equiv}N\cdots H$ bonding and proton exchange behavior with $-NH_3^+$ and NH_2, which was inefficient for **TCNA-DAP** entity. The DFT studies also confirm this observation. The emission shifts with intensity enhancement were monitored by WAXS studies that offer a variation in the diffraction pattern with a gradual development of well-diffracted signals. Finally, coverslip/Al-coated silica-gel/paper-based platforms were substantiated to successfully detect the freshness of chicken and fish. The same platform would be perfect for determining the spoiled protein-rich food at different stages of putrefaction, preventing food waste, and enriching the food safety solution.

Author contributions

Madhuparna performed all the reactions, conducted all the experiments, and presented. The manuscript draft was partially prepared. Manab designed the molecule, analyzed the results, and prepared the final manuscript. PKS and PS performed the DFT/TDDFT studies and generated the relevant figures.

Conflicts of interest

There are no conflicts to declare.

Acknowledgements

We thank LSRB [389/FSH&ABB/2021] for financial support. Special thanks: BITS-Pilani Hyderabad Campus X-ray diffraction and NMR facility are acknowledged. Special thanks to Prof. Aravind Raghavan for helping collect and process WAXS data and fruitful discussions. MC thanks BITS-Pilani Hyderabad Campus for MC's fellowship. We thank Dr. Suman for helping us solve the crystal structure.

References

1 R. Jia, W. Tian, H. Bai, J. Zhang, S. Wang and J. Zhang, Amine-responsive cellulose-based ratiometric fluorescent materials for real-time and visual detection of shrimp and crab freshness, *Nat. Commun.*, 2019, **10**, 1–8.
2 S. K. Kannan, B. Ambrose, S. Sudalaimani, M. Pandiaraj, K. Giribabu and M. Kathiresan, A review on chemical and electrochemical methodologies for the sensing of biogenic amines, *Anal. Methods*, 2020, **12**, 3438–3453.
3 R. S. Andre, L. A. Mercante, M. H. M. Facure, R. C. Sanfelice, L. Fugikawa-Santos, T. M. Swager and D. S. Correa, Recent Progress in Amine Gas Sensors for Food Quality Monitoring: Novel Architectures for Sensing Materials and Systems, *ACS Sens.*, 2022, **7**, 2104–2131.
4 T. Gao, E. S. Tillman and N. S. Lewis, Detection and Classification of Volatile Organic Amines and Carboxylic Acids Using Arrays of Carbon Black-Dendrimer Composite Vapor Detectors, *Chem. Mater.*, 2005, **17**, 2904–2911.
5 N. Kaur, S. Chopra, G. Singh, P. Raj, A. Bhasin, S. K. Sahoo, A. Kuwar and N. Singh, Chemosensors for biogenic amines and biothiols, *J. Mater. Chem. B*, 2018, **6**, 4872–4902.
6 M. Gao, S. Li, Y. Lin, Y. Geng, X. Ling, L. Wang, A. Qin and B. Z. Tang, Fluorescent Light-Up Detection of Amine Vapors Based on Aggregation-Induced Emission, *ACS Sens.*, 2016, **2**, 179–184.
7 H. Ye, S. Koo, B. Zhu, Y. Ke, R. Sheng, T. Duan, L. Zeng and J. S. Kim, Real-Time Fluorescence Screening Platform for Meat Freshness, *Anal. Chem.*, 2022, **94**, 15423–15432.

8 (*a*) M. Schirone, L. Esposito, F. D'Onofrio, P. Visciano, M. Martuscelli, D. Mastrocola and A. Paparella, Biogenic Amines in Meat and Meat Products: A Review of the Science and Future Perspectives, *Foods*, 2022, **11**, 788–812; (*b*) B. del Rio, B. Redruello, D. L. M. Linares, V. Ladero, P. R. Madiedo, M. Fernandez, M. C. Martin and M. A. Alvarez, The biogenic amines putrescine and cadaverine show in vitro cytotoxicity at concentrations that can be found in foods, *Sci. Rep.*, 2019, **9**, 120.

9 A. I. Danchuk, N. S. Komova, S. N. Mobarez, S. Y. Doronin, N. A. Burmistrova, A. V. Markin and A. Duerkop, Optical sensors for determination of biogenic amines in food, *Anal. Bioanal. Chem.*, 2020, **412**, 4023–4036.

10 L. Jiang, H. Ye, D. Ma, J. Rodrigues, R. Sheng and D. Min, A smartphone-adaptable fluorescent sensing tag for non-contact and visual monitoring of the freshness of fish, *Analyst*, 2022, **147**, 923–931.

11 M. Ikeda, T. Yoshii, T. Matsui, T. Tanida, H. Komatsu and I. Hamachi, Montmorillonite– supramolecular hydrogel hybrid for fluorocolorimetric sensing of polyamines, *J. Am. Chem. Soc.*, 2011, **133**, 1670–1673.

12 L. Wunderlichová, L. Buňková, M. Koutný, P. Jančová and F. Buňka, Formation, degradation, and detoxification of putrescine by foodborne bacteria: a review, *Compr. Rev. Food Sci. Food Saf.*, 2014, **13**, 1012–1030.

13 K. Saeki, K. Ikari, H. Yokoi, S.-I. Ohira, H. Okochi and K. Toda, Biogenic Diamines and Their Amide Derivatives Are Present in the Forest Atmosphere and May Play a Role in Particle Formation, *ACS Earth Space Chem.*, 2022, **6**, 421–430.

14 A. Onal, A review: current analytical methods for the determination of biogenic amines in foods, *Food Chem.*, 2007, **103**, 1475–1486.

15 M. Papageorgiou, D. Lambropoulou, C. Morrison, E. Kłodzinska, J. Namiesnik and J. Płotka-Wasylka, *TrAC, Trends Anal. Chem.*, 2018, **98**, 128–142.

16 N. Verma, V. Hooda, A. Gahlaut, A. Gothwal and V. Hooda, Literature update of analytical methods for biogenic amines determination in food and beverages, *Crit. Rev. Biotechnol.*, 2020, **40**, 1–14.

17 (*a*) Z. Song, M. Cai, Y. Zhao, M. Jin and S. Deng, Simultaneous determination of 14 biogenic amines and metabolites in bullfrog blood using UFLC-MS/MS with SPE, *Anal. Methods*, 2015, **7**, 7436–7442; (*b*) R. L. Self, W.-H. Wu and H. S. Marks, Simultaneous quantification of eight biogenic amine compounds in tuna by matrix solid-phase dispersion followed by HPLC–orbitrap mass spectrometry, *J. Agric. Food Chem.*, 2011, **59**, 5906–5913.

18 G. Munzi, S. Failla and S. D. Bella, Highly selective and sensitive colorimetric/fluorometric dual mode detection of relevant biogenic amines, *Analyst*, 2021, **146**, 2144–2151.

19 B. Prusti, S. Tripathi, A. Jain and M. Chakravarty, Concentration-Guided Visual Detection of Multiphase Aliphatic Biogenic Amines through Amine–Phenol Recognition Using a Dual-State Emitter, *ACS Appl. Mater. Interfaces*, 2023, **15**, 16492–16504.

20 R. Roy, A. Pramanik, T. Dutta, V. Sharma, Kovida and A. L. Koner, Harnessing solution and solid-state emissive materials from aliphatic biogenic amine-induced transient assembly and spontaneous disassembly, *Mater. Chem. Front.*, 2022, **6**, 3489–3503.

21 L. Zeng, X. Xiao, H. Ye, D. Ma and J. Zhou, Fast visual monitoring of the freshness of beef using a smart fluorescent sensor, *Food Chem.*, 2022, **394**, 133489.

22 B. Zhu, L. Jiang, T. Chen, G. Bao, L. Zeng, X. Hu and H. Yuan, A colorimetric and fluorescence lighting-up probe for the determination of biogenic primary diamine during the spoilage of fish, *Dyes Pigm.*, 2021, **186**, 108963.

23 S. Sentellas, Ó. Núñez and J. Saurina, Recent Advances in the Determination of Biogenic Amines in Food Samples by (U)HPLC, *J. Agric. Food Chem.*, 2016, **64**, 7667–7678.

24 H. Ahangari, S. Kurbanoglu, A. Ehsani and B. Uslu, Latest trends for biogenic amines detection in foods: enzymatic biosensors and nanozymes applications, *Trends Food Sci. Technol.*, 2021, **112**, 75–87.

25 M. Venkateswarulu, P. Gaur and R. R. Koner, Sensitive molecular optical material for signaling primary amine vapors, *Sens. Actuators, B*, 2015, **210**, 144–148.

26 S. Mallick, F. Chandra and A. L. Koner, A ratiometric fluorescent probe for detection of biogenic primary amines with nanomolar sensitivity, *Analyst*, 2016, **141**, 827–831.

27 L. Wang, S. Xin, C. Zhang, X. Ran, H. Tang and D. Cao, Development of a novel chromophore reaction-based fluorescent probe for biogenic amines detection, *J. Mater. Chem. B*, 2021, **9**, 9383–9394.

28 Z. Jiao, Y. Zhang, W. Xu, X. T. Zhang, H. B. Jiang, P. C. Wu, Y. Y. Fu, Q. G. He, H. M. Cao and J. G. Cheng, Highly Efficient Multiple-Anchored Fluorescent Probe for the Detection of Aniline Vapor Based on Synergistic Effect: Chemical Reaction and PET, *ACS Sens.*, 2017, **2**, 687–694.

29 P. Alam, N. L. C. Leung, H. Su, Z. Qiu, R. T. K. Kwok, J. W. Y. Lam and B. Z. Tang, A highly sensitive bimodal detection of amine vapours based on aggregation induced emission of 1,2-dihydroquinoxaline derivatives, *Chem. – Eur. J.*, 2017, **23**, 14911–14917.

30 R. Roy, N. R. Sajeev, V. Sharma and A. L. Koner, Aggregation induced emission switching based ultrasensitive ratiometric detection of biogenic diamines using a perylenediimide-based smart fluorophore, *ACS Appl. Mater. Interfaces*, 2019, **11**, 47207–47217.

31 L. Li, W. Li, X. Ran, L. Wang, H. Tang and D. Cao, A highly efficient, colorimetric and fluorescent probe for recognition of aliphatic primary amines based on a unique cascade chromophore reaction, *Chem. Commun.*, 2019, **55**, 9789–9792.

32 A. Orouji, F. Ghasemi, A. Bigdeli and M. R. Hormozi-Nezhad, Providing multicolor plasmonic patterns with Au@ Ag core–shell nanostructures for visual discrimination of biogenic amines, *ACS Appl. Mater. Interfaces*, 2021, **13**, 20865–20874.

33 F. Kong, Y. Mu, X. Zhang, Q. Lu, Z. Yang, J. Yao and L. Zhao, A novel fluorescent probe of alkyne compounds for putrescine detection based on click reaction, *RSC Adv.*, 2022, **12**, 26630–26638.

34 X. Qi, W.-F. Wang, J. Wang, J.-L. Yang and Y.-P. Shi, Highly selective colorimetric detection of putrescine in fish

products using o-phthalaldehyde derivatization reaction, *Food Chem.*, 2018, **259**, 245–250.

35 J. L. B. Vázquez, Y. A. A. Sánchez, L. A. R. Cortés and B. R. Molina, Dual-state emission (DSE) in organic fluorophores: design and applications, *Chem. Mater.*, 2021, **33**, 7160–7184.

36 F. Yu, H. Zhao, Y. Li, G. Xia and H. Wang, D–A-Type fluorophores with efficient dual-state emission for imaging at ultralow concentration, *Mater. Chem. Front.*, 2022, **6**, 155–162.

37 M. Chakraborty and M. Chakravarty, Variation in solvato-, AIE-and mechano-fluorochromic behavior for furanyl and thiophenyl-substituted anthranyl π-conjugates: the role of tiny flanking donor groups, *Mater. Adv.*, 2021, **2**, 6418–6427.

38 (*a*) M. Chakraborty and M. Chakravarty, Varied Optical features and mechanofluorochromism in dicyanovinyl *vs.* cyanoacrylicacid-linked twisted π-conjugates: a potential reusable platform for security applications, *Mater. Today Chem.*, 2024, **35**, 101836–101845; (*b*) M. Chakraborty and M. Chakravarty, Flanking-donor-controlled diversity in mechanical-force-induced reversible fluorochromism and enhanced emission for carboxylic acid and ester linked solid-state emitters, *CrystEngComm*, 2023, **25**, 1126–1135.

39 L. Wang, X. Ran, H. Tang and D. Cao, Recent advances on reaction-based amine fluorescent probes, *Dyes Pigm.*, 2021, **194**, 109634.

40 A. R. Longstreet, M. Jo, R. R. Chandler, K. Hanson, N. Zhan, J. J. Hrudka, H. Mattoussi, M. Shatruk and D. T. McQuade, Ylidenemalononitrile enamines as fluorescent "turn-on" indicators for primary amines, *J. Am. Chem. Soc.*, 2014, **136**, 15493–15496.

41 Y. Hu, T. Han, N. Yan, J. Liu, X. Liu, W.-X. Wang, J. W. Y. Lam and B. Z. Tang, Visualization of Biogenic Amines and In Vivo Ratiometric Mapping of Intestinal pH by AIE-Active Polyheterocycles Synthesized by Metal-Free Multicomponent Polymerizations, *Adv. Funct. Mater.*, 2019, **29**, 1902240.

42 H. Ye, Y. Ke, W. Li, B. Zhu, L. Jiang, X. Hu and L. Zeng, Molecular engineering of fluorescence probe for real-time non-destructive visual screening of meat freshness, *Anal. Chim. Acta*, 2023, **1254**, 341125.

43 D. R. Turner, A. J. Edwards and R. O. Piltz, Nitrile groups as hydrogen-bond acceptors in a donor-rich hydrogen-bonding network, *CrystEngComm*, 2012, **14**, 6447–6464.

44 P. Zhou, P. Li, Y. Zhao and K. Han, Restriction of flip-flop motion as a mechanism for aggregation-induced emission, *J. Phys. Chem. Lett.*, 2019, **10**, 6929–6935.

45 C. Zhu, R. T. K. Kwok, J. W. Y. Lam and B. Z. Tang, Aggregation-induced emission: a trailblazing journey to the field of biomedicine, *ACS Appl. Bio Mater.*, 2018, **1**, 1768–1786.

46 (*a*) J. Kumpf, J. Freudenberg, K. Fletcher, A. Dreuw and U. H. F. Bunz, Detection of amines with extended distyrylbenzenes by strip assays, *J. Org. Chem.*, 2014, **79**, 6634–6645; (*b*) G. Zhang, A. S. Loch, J. C. M. Kistemaker, P. L. Burn and P. E. Shaw, Dicyanovinyl-based fluorescent sensors for dual mechanism amine sensing, *J. Mater. Chem. C*, 2020, **8**, 13723–13732.

47 Z. Wen, L. J. Karas, C.-H. Wu, I. Judy and C. Wu, How does excited-state antiaromaticity affect the acidity strengths of photoacids?, *Chem. Commun.*, 2020, **56**, 8380–8383.

48 K. J. Nelson, P. J. Brown, H. E. Rudel and K. Takematsu, Divergent excited state proton transfer reactions of bifunctional photoacids 1-ammonium-2-naphthol and 3-ammonium-2-naphthol in water and methanol, *Phys. Chem. Chem. Phys.*, 2019, **21**, 24383–24392.

49 L. Wang, S. Xin, C. Zhang, X. Ran, H. Tang and D. Cao, Development of a novel chromophore reaction-based fluorescent probe for biogenic amines detection, *J. Mater. Chem. B*, 2021, **9**, 9383–9394.

50 (*a*) R. M. Silverstein, F. X. Webster and D. J. Kiemle, *Spectrometric Identification of Organic compounds*, John Wiley & Sons, 7th edn, 2005, pp. 102–103; (*b*) B. C. Smith, *Spectroscopy*, 2018, **33**(1), 14–20.

51 B. C. Smith, *Spectroscopy*, 2019, **34**(7), 18–21.

52 N. Ziao, J. Graton, C. Laurence and J.-Y. Le Questel, Amino and cyano N atoms in competitive situations: which is the best hydrogen-bond acceptor? A crystallographic database investigation, *Acta Cryst.*, 2001, **B57**, 850–858.

53 D. R. Turner, A. J. Edwards and R. O. Piltz, Nitrile groups as hydrogen-bond acceptors in a donor-rich hydrogen-bonding network, *CrystEngComm*, 2012, **14**, 6447–6451.

54 J.-Y. Le Questel, M. Berthelot and C. Laurence, Hydrogen-bond acceptor properties of nitriles: a combined crystallographic and ab initio theoretical investigation, *J. Phys. Org. Chem.*, 2000, **13**, 347–358.

55 S. Yang, S. Zhou, H. Li, Y. Nie, H. Xu, W. Liu, J. Miao, Y. Li, G. Gao, J. You and X. Jiang, Multistimuli-responsive squaraine dyad exhibiting concentration-controlled vapochromic luminescence, *ACS Appl. Mater. Interfaces*, 2022, **14**, 16611–16620.

56 Y. Q. Dong, C. Li, W. Zhao, Y. Dong and B. Z. Tang, Stimulus responsive luminescent materials: crystallization-induced emission enhancement, *J. Mol. Eng. Mater.*, 2013, **01**, 1340010–1340013.

57 G. Liao, J. Zhang, X. Zheng, X. Jia, J. Xu, F. Zhao, N. Wang, K. Liu, P. Chen and X. Yin, Crystallization-induced emission enhancement of highly electron-deficient dicyanomethylene-bridged triarylboranes, *Chem. Commun.*, 2021, **57**, 7926–7929.

58 Takeshi Yanai, D. P. Tew and N. C. Handy, A new hybrid exchange–correlation functional using the Coulomb-attenuating method (CAM-B3LYP), *Chem. Phys. Lett.*, 2004, **393**, 51–57.

59 M. J. Frisch, G. W. Trucks, H. B. Schlegel and G. E. Scuseria *et al.*, *Gaussian 09, Revision D.02*, Gaussian, Inc., Wallingford CT, 2009.

60 M. D. Hanwell, D. E. Curtis, D. C. Lonie, T. Vandermeerschd, E. Zurek and G. R. Hutchison, Avogadro: an advanced semantic chemical editor, visualization, and analysis platform, *J. Cheminf.*, 2012, **4**, 1–17.